# Application of LEDs in Intravascular Photoacoustic Imaging

Dorian Tricaud
Department of Electrical and Computer Engineering
University of Illinois Urbana-Champaign

April 22, 2024

# I Abstract

The goal of this project is to use the Crosslight APSYS© software to create a set of LEDs capable of performing photoacoustic imaging. By using InGaN and InGaAs multi-quantum well structures, green and infrared wavelengths capable of imaging blood vessels and other organic compounds were achieved. Then to achieve power output capable of high-resolution, the power output of the device under high-current injection was modeled. Under high-current injection temperature began to become an important variable, thus the thermal generation of the device was characterized. It became apparent that some form of temperature regulation was necessary, which was resolved via a heat sink on the bulk of the material.

# II Introduction

Medical Imaging has revolutionized the way we understand and diagnose diseases, offering a unique perspective into the inner workings of the human body. From the discovery of X-rays back in 1895 to the established technologies of today, such as MRI and CT scans, medical imaging has continuously pushed the boundaries of what is possible in medicine. Medical imaging provides doctors with invaluable information, enabling accurate diagnoses and providing clarity during surgical operations.

The discovery of the X-ray in 1895 by Wilhelm Conrad Röentgen is often regarded as the birth of medical imaging. For the first time in history, physicians had access to the inside of their patient without the need for surgery. The first X-ray image was the hand of Röentgen's wife (See Figure 1), demonstrating the ability of X-rays to penetrate soft tissue and provide images of bones. Within a few days, news of the discovery spread worldwide nicknamed 'wonder rays' with the potential to revolutionize medicine. X-rays were quickly adopted for use in dental imaging and bone fractures, later being brought to the front lines of World War 1 to treat soldiers[1, 2].

Figure 1: A print of one of the first X-rays by Röntgen [2]

The main drawback of X-rays is that they provide a 2-dimensional single-plane image of body

structures. This leads to various issues when organs overlap or if they have a similar density. In order to resolve these issues, computed tomography (CT) was developed in 1967 using multiple X-ray angles to provide additional perspectives. These additional perspectives are arranged via computer software to generate a volume image. This imaging was so revolutionary that 'by the early 1980s, more than three million CT studies had been performed. Presently that number has grown to well over 100 million CT studies annually' [3]. This technology has been continuously developed and tuned to improve the safety and quality of its imaging[1].

A few years after the development of the CT scan, a new imaging technology known as magnetic resonance imaging (MRI) was published. As its name suggests, it uses magnets rather than x-rays to generate images. By generating extremely large magnetic fields around a sample of interest, individual atoms begin to align to this externally generated field. Then by supplying the atoms with energy via radio waves, one can measure the response of the aligned atoms to produce an image. It provides exceptional soft-tissue contrast making it a popular imaging technique for soft tissue applications [1].

One of the drawbacks to CT and MRI scans is that their machines are expensive to purchase, operate, and maintain. As a result, they can be difficult to find in rural and lower-income areas. An alternative to these machines is the ultrasound technology, which as the name implies uses sound waves (typically high frequency) to image the body. These sound waves echo off various parts of the body and based on the return time and amplitude, an image can be reconstructed. It operates using a relatively small machine, meaning that it can be used face to face for patients, commonly experienced during fetal ultrasounds. Despite the small size, it can still be used for more extensive imaging with the use of contrasting injection agents. These agents improve the image quality by improving the echo capabilities of the sample[1, 4].

Photoacoustic imaging is a relatively new imaging technique built upon similar principles to the ultrasound, with the primary difference being it generates optical waves rather than sound waves. This technology uses the photoacoustic effect and generated electromagnetic radiation to produce measurable ultrasound waves. The photoacoustic effect, first discovered in 1880 by Alexander Graham Bell, details the generation of ultrasonic waves by various materials whenever they absorb light. Over a century later, in 1993, the first medical study using the photoacoustic effect was published. Using a 1064 nm laser, a human finger was imaged successfully isolating signals from the fingernail and bone underneath. Modern applications have been able to 'provide an exact reconstruction for spherical, cylindrical, and planar geometries' [5], with the only practical limiting factor being the computational speed required to process the photoacoustic signals. The main drawback of a photoacoustic imaging system is that, like MRI and CT scans, it relies on machinery that is expensive to purchase, operate, and maintain. Some preliminary research has found success replacing the laser system with an LED-based system, estimating the LED system to cost approximately 10 times less than the laser system [5, 6, 7].

Intravascular Photoacoustic Imaging (IVPA) is a special form of photoacoustic imaging that uses catheters to operate within blood vessels. This type of imaging provides a unique perspective enabling high-resolution imaging of various plaques and even their composition. These images provide invaluable information to doctors, decreasing uncertainty in diagnoses and identifying treatment plans that best fit the issue at hand. An additional benefit of IVPA is the ability to measure various vital signs via wavelength modulation. By adjusting the wavelength emitted by the laser,

medical staff can determine metrics such as oxygen content, blood flow rate, and macrophage count. IVPA suffers similar cost drawbacks to a regular photoacoustic system, oftentimes even more so because of the specialized nature of the machinery [8]. This project aims to explore the possibility of using an LED based catheter for intravascular photoacoustic imaging, reducing the costs and increasing the availability of IVPA techniques.

# III Technical Background

An LED is most often constructed using quantum well(s) sandwiched between p and n doped bulk material with a band-gap higher than the quantum well. This sandwich creates confinement in the QW, resulting in the formation of quantum states within the energy band structure. These quantum states help promote recombination, increasing the efficiency of the LED overall. A simple QW LED structure can be seen in Figure 2, where GaAs is sandwiched with $Al_{0.3}Ga_{0.7}As$. This sandwich formed discrete energy levels $E_1$ and $E_h$ within the quantum well, other higher energy levels exists however are less likely to be occupied by carriers.

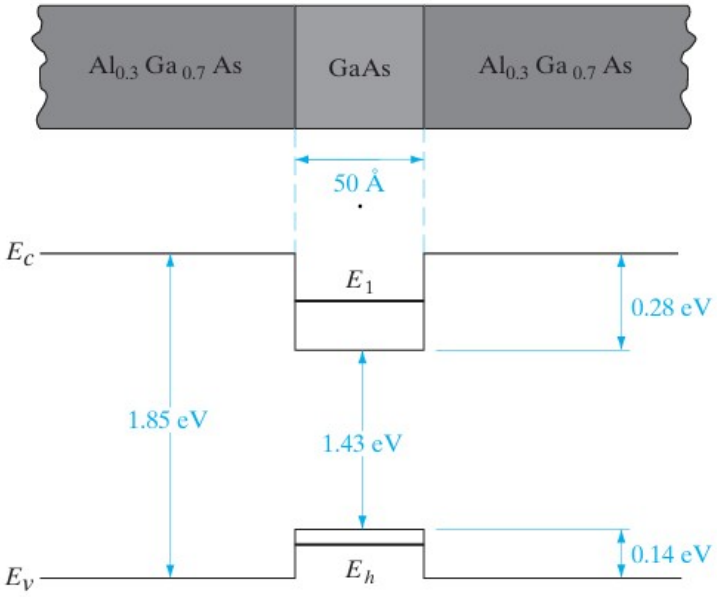


Figure 2: Energy Band Diagram of QW Structure [9].

Whenever carriers are injected into an LED (via current), they mostly recombine in the quantum well resulting in photonic output. However, there are other forms of recombination that do not emit any light. This recombination is often characterized using the A-B-C model, which assigns coefficients to model each form of recombination. The $A$-term represents Shockley-Reed-Hall recombination, which typically dominates at lower levels of injection. The $B$-term represents the radiative forms of recombination, which occurs at all levels of injection. The $C$-term represents Auger Recombination, which becomes relevant at higher levels of injection. These 3 coefficients are related via the equation below Equation 1, where $R$ is recombination rate and $\Delta n$ is the excess

carrier concentration in the material. This equation captures the general trends of each coefficient with $A$ dominating when $\Delta n$ is smaller, and $C$ dominating when $\Delta n$ is larger.

$$R = A(\Delta n) + B(\Delta n)^2 + C(\Delta n)^3 \tag{1}$$

The internal quantum efficiency (IQE) of an LED can be described by how many photons the active layer emits for the amount of electrons that is injected. Using the A-B-C model, the equation for IQE can be seen below in Equation 2, which is simply the radiative recombination over the total recombination.

$$\eta_{IQE} = \frac{B(\Delta n)^2}{A(\Delta n) + B(\Delta n)^2 + C(\Delta n)^3} \tag{2}$$

A more realistic efficiency measure of an LED is the external quantum efficiency (EQE) of the device, which includes losses due to packaging materials and reflection. This value can be easily calculated by multiplying the IQE and LEE (light extraction efficiency) together.

LEE can be calculated with the refractive index of the materials used in the device as well as the output medium. For this calculation we use the equation below, Equation 3. Where $n_s$ is the refractive index of the semiconductor, $n_e$ is the refractive index of the epoxy, and $n_o$ is the refractive index of the output medium. This equation calculates the single-cone extraction value, for each LED there can be up to 6 cones of extraction depending on the encapsulation shape.

$$\eta_{extraction} = \frac{1 - \sqrt{1 - (n_e/n_s)^2}}{2} \times \frac{4 n_s n_e}{(n_s + n_e)^2} \times \frac{4 n_e n_o}{(n_e + n_o)^2} \tag{3}$$

The current injection to generate photons also results in heating of the device. For the Crosslight APSYS© software, it captures heat generation and flow via mathematical formulas. The flow of heat through the device is modeled using the formula below, Equation 4.

$$J_h = -\kappa \nabla T \tag{4}$$

Where $J_h$ is the heat flux of the device, $\kappa$ is the thermal conductivity of the material, and $T$ is the temperature profile throughout the device.

The temperature gradient of the device induces an electron and hole current in the forms derived below, Equations 5 6.

$$I_e = -q \mu_n n P_n \nabla T \tag{5}$$

$$I_p = -q \mu_p p P_p \nabla T \tag{6}$$

$P_n$ and $P_p$ are defined as the thermoelectric powers of the device and are given by their own formulas below, Equations 7 8.

$$P_n = \frac{k_B}{q}[-\frac{5}{2} - v + \ln(\frac{n}{N_c})] \tag{7}$$

$$P_p = \frac{k_B}{q}[-\frac{5}{2} - v + \ln(\frac{p}{N_v})] \tag{8}$$

Where $v$ is the exponent used in the field-dependent relaxation time, for phonon scattering $v = -\frac{1}{2}$ [10].

The Crosslight APSYS© software utilizes 5 mathematical models, to characterize heat generation. These models are separated into joule/optical heat, generation/recombination heat, and Thomson/Peltier heat. During the simulations, the relevant sources of heat generation were joule/optical and generation/recombination. Those sources are explained below.

Joule and Optical heating comes from the steady-state and frequency components of current within the semiconductor device. It is modeled using the equations below, Equations 9 10

$$H_{joule-dc} = \frac{J_n^2}{q\mu_n n} + \frac{J_p^2}{q\mu_p p} \tag{9}$$

$$H_{joule-ac} = \frac{\epsilon_2 \epsilon_0 \omega F_{op}^2}{k_0} \tag{10}$$

Where $F_{op}$ is the root-mean-square of the electric field within the device, $\epsilon_2$ is the optical dielectric coefficient, and $\omega$ is the angular frequency of the optical wave.

An additional form of heat comes from the recombination of carriers within the device. This is modeled using Equation 11:

$$H_{rec} = (R_{trap} + R_{Aug} + R_{spon} + R_{stim})(E_{fn} - E_{fp}) + qR_{total}T(P_p - P_n) \tag{11}$$

Where $P_p$ and $P_n$ were previously defined in Equations 7 8.

A small amount of cooling comes in the form of radiative heat, in which photons absorb some thermal energy to escape the material, removing that thermal energy from the device. This term is modeled by Equation 12 below.

$$H_{rad} = -(R_{stim} + R_{spon})\hbar\omega \tag{12}$$

$H_{rec}$ and $H_{rad}$ are typically similar in magnitude and often cancel each other out. Thus, the main contribution of heating is the $H_{joule}$ term.

With the physical characteristics of the LED reviewed, the role of optic devices in photoacoustic

imaging can be examined.

Photoacoustic imaging involves two core components, the ultrasonic sensor and the light source. For this project, only the light source aspect was considered and modeled. The light source, traditionally a solid-state laser system but can be any source of light, irradiates tissue causing it to thermally fluctuate. These thermal variations result in the tissue slightly expanding and contracting, generating small pressure waves as these changes occur. The amplitude, direction, and delay of these pressure waves can be interpreted by the sensor and computer in order to reconstruct the material. The mathematical equation that governs this behavior is detailed below.

The pressure generated by the absorption sample, $P_0$ can be expressed by Equation 13.

$$P_0 = \gamma \mu_a F \tag{13}$$

Where $\mu_a$ is the absorption coefficient of the sample and $F$ is the optical fluence illuminating the sample.

$\gamma$ is known as the Gröneisen coefficient, a 'thermodynamic constant that provides a measure of the conversion efficiency of heat energy to pressure' [5], which is defined below, Equation 14.

$$\gamma = \frac{\beta}{\kappa \rho C_p} \tag{14}$$

With $\beta$ being the isobaric volume expansion coefficient, $\kappa$ being the isothermal compressibility, $C_p$ being the specific heat, and $rho$ being the mass density. All these terms are defined by the sample absorbing optical waves [11].

Intravascular Photoacoustic Imaging follows the same behavior as described above, the main differences being the use of optic fiber in a catheter to transmit the optical energy. In addition, the imaging medium of blood rather than skin and air changes the viable optical wavelengths for imaging. A graph of absorption coefficients vs. wavelength for intravascular photoacoustic imaging is displayed below, Figure 3.

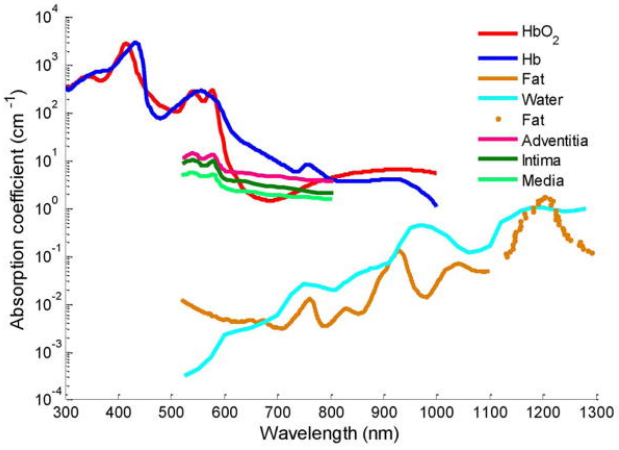


Figure 3: Absorption Coefficients for Intravascular Photoacoustic Imaging [8]

# IV Simulation Results and Discussion

The behavior of LEDs was characterized via the Crosslight APSYS © software.

To be used in intravascular photoacoustic imaging, the most important metrics are the temperature and power output of the LED device. Some useful secondary metrics include the temperature profile across the device and also the IQE. A typical catheter used in medical operations is approximately 1 mm in diameter [8], as such the width of the device was limited to 1000um in order to satisfy this constraint. In addition, in the interest of maximum power output for resolution size, we ranged the injected current density from 0 A/m to 900 A/m for each device. The current injection simulation stops at 900 A/m due to simulation limitations. This corresponds to approximately 1 to 15 A being injected into the scaled device, much lower than practical applications which could reach upwards of 130 A [12]. Wavelengths selected for the LED were pulled from various modern laser-based intravascular photoacoustic applications in order to get a reasonable spread of values and also determine the feasibility of imaging certain compounds [13, 14]. GaN/InGaN QW structures were used for wavelengths within the visible light spectrum, while GaAs/InGaAs QW structures were used for the infrared light spectrum. Initial guesses of compositions were calculated using Vegard's law and online parameters. These guesses were tuned in the software until the desired peak wavelength was reached. A table of the wavelength and final material information can be seen below in Table 1.

| Wavelength | Material |
|---|---|
| 530 nm | $In_{0.32}Ga_{0.68}N$ |
| 630 nm | $In_{0.43}Ga_{0.57}N$ |
| 1070 nm | $In_{0.57}Ga_{0.43}As$ |
| 1210 nm | $In_{0.77}Ga_{0.23}As$ |

Table 1: Wavelength and Material Information for APSYS Simulation

## IV.1 Heat Sink Design

During the initial stages of the project it became apparent that a heat sink would be necessary to dissipate the heat generated by the LED device. Initial design iterations attempted to use the contacts themselves as a heat sink, but did not dissipate enough heat at high currents. The next approach was to add a thermal contact to the p and n regions of the device, initially set with a thickness of 2 um. This approach did see a significant reduction in temperature, but still did not dissipate enough heat. There was an attempt to apply an external material next to the bulk in order to conduct heat away, however, this material affected the current flow throughout the device ultimately resulting in large power output drops. The solution presented in this report was to increase the thickness of the n and p regions to 10 um. Although it increased overall recombination in the device the added surface area proved invaluable in lowering the maximum temperature of the device. Below is an image displaying the temperature characteristics of the device, Figure 4. Additionally, the contacts were reduced to half the width of the device to provide potential space for

routing and an additional surface for heat sink application, this additional heat sink is not simulated or captured in this report.

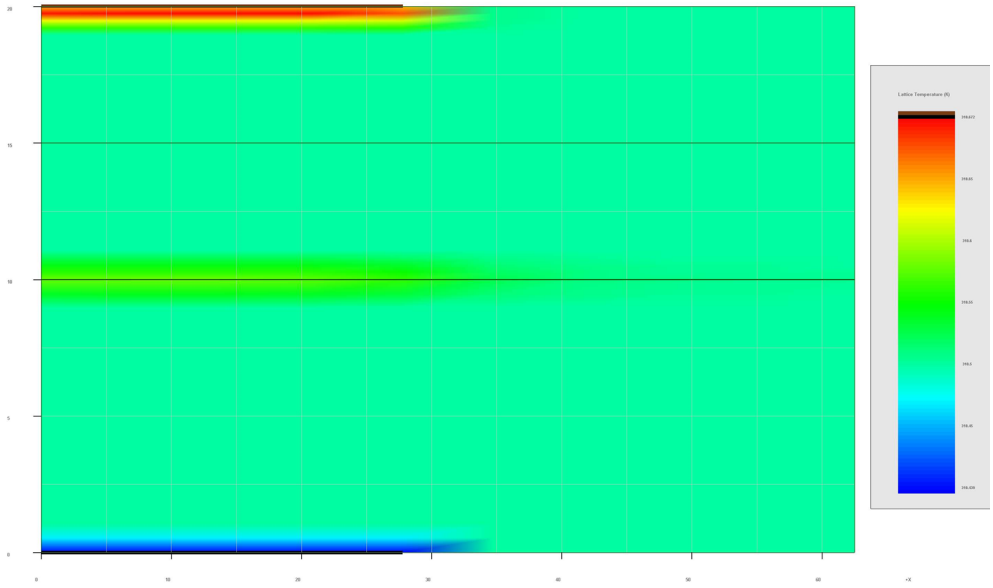

Figure 4: General Temperature Diagram. Red - Warmer. Blue - Cooler.

The LED structure utilized 2 quantum wells sandwiched between two large bulk regions. A diagram of the device can be seen below, Figure 5.

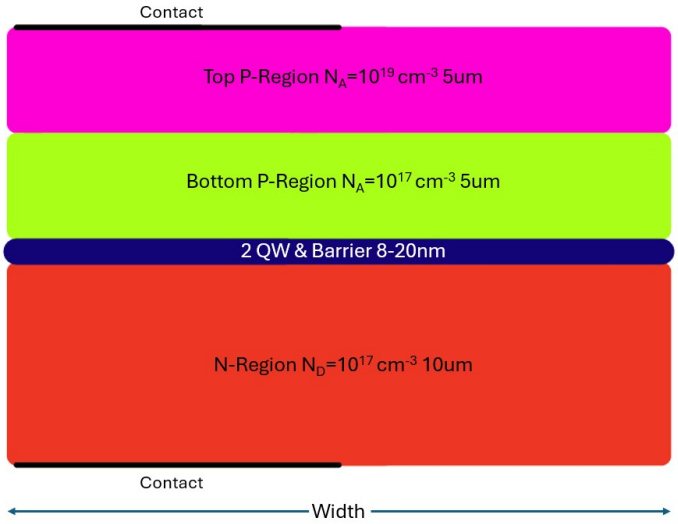


Figure 5: General Structure of Device.

The QWs are 2 nm in thickness. The barrier regions ranged between 3 nm to 10 nm in thickness. The 10 um p-region is separated into 2 regions with doping concentrations of $N_A = 10^{19}\text{cm}^{-3}$ and $N_A = 10^{17}\text{cm}^{-3}$ for the top and bottom regions, respectively. The 10 um n-region is doped with $N_D = 10^{18}\text{cm}^{-3}$. Contacts are on the top and bottom cell with half the device length.

The band structure of the QW region for the 630 nm wavelength, 1000 um width device can also be seen below, Figure 6.

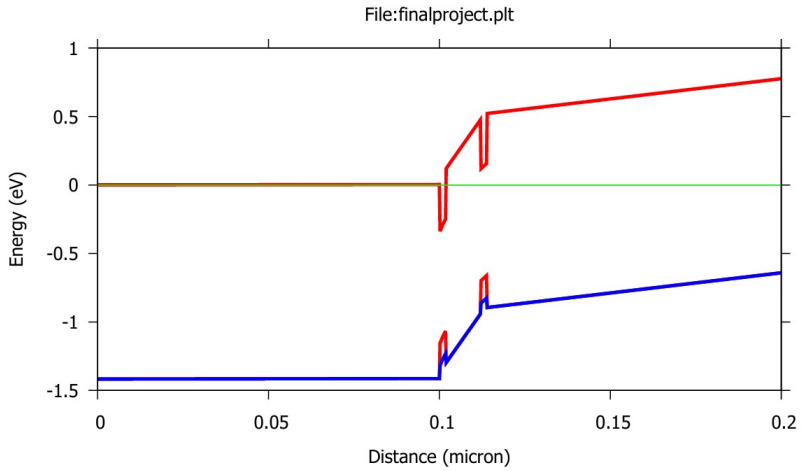


Figure 6: QW Band Diagram for 1070 nm wavelength, 1000 um width.

To determine the power output of the device, we need a metric for the light extraction efficiency of the device. Using Equation 3 and material properties [15, 16], we calculated the LEE below in Table 2. Blood has a refractive index of about 1.36 [17]. This is assuming 3-4 cones of output for each device.

| Bulk | Refractive Index | Epoxy | Refractive Index | Approximate LEE |
|---|---|---|---|---|
| GaN | 2.38 | ZnO | 1.87 | 72% |
| GaAs | 3.51 | TiO2 | 2.28 | 45% |

Table 2: LEE for devices

## IV.2 Sizing Effects on IQE, Temperature, and Output Power

The effects of LED sizing on IQE, Output Power, and Temperature is detailed in this subsection of the report. IQE of an LED is dependent on a variety of factors, with the general equation being described in Equation 2. To explore the dependence of IQE on device width, a set of simulations ranged the width of the device from 62.5 um up to 1000 um. Figure 7 shows the variation in IQE for the 1210 nm wavelength LED. Across all LEDs there is an obvious trend that IQE decreases as current injection increases. This is mostly attributed to the current density droop, which is the domination of auger recombination at high current injection. Another source of this current density droop can be attributed to the thermal effects, which decrease IQE as temperature increases.

Alongside this current droop, it is observed that the IQE decreases as device size decreases. This is also an effect of the current density droop, since smaller device dimensions results in a larger current density within the device. In addition, surface effects play a larger role at smaller device sizes further decreasing the IQE.

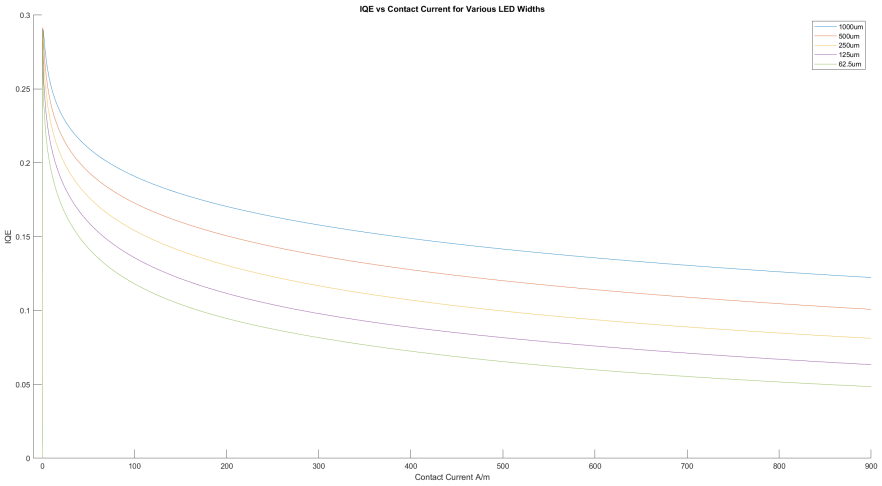


Figure 7: IQE vs Current Injection for 1210 nm LED with Various Device Widths

Temperature is theoretically inversely proportional to IQE, as such it is expected that a correlation will present itself during simulation. Once again, to explore the dependence of temperature on device width, a set of simulations ranged the width of the device from 62.5 um to 1000 um. All the designs utilized the final heat sink detailed in the previous Subsection IV.1. Figure 8 shows the variation in max temperature for the 1210 nm wavelength LED. Across all LEDs, as the current increases the temperature of the device also increases, confirming the inverse relationship between IQE and temperature. Additionally, the overall temperature of devices increases as device size decreases, once again displaying an inverse relationship with IQE. One interesting part of the graph is that it isn't perfectly linear, suggesting that injecting more current past the simulated value would drastically increase the temperature of the device.

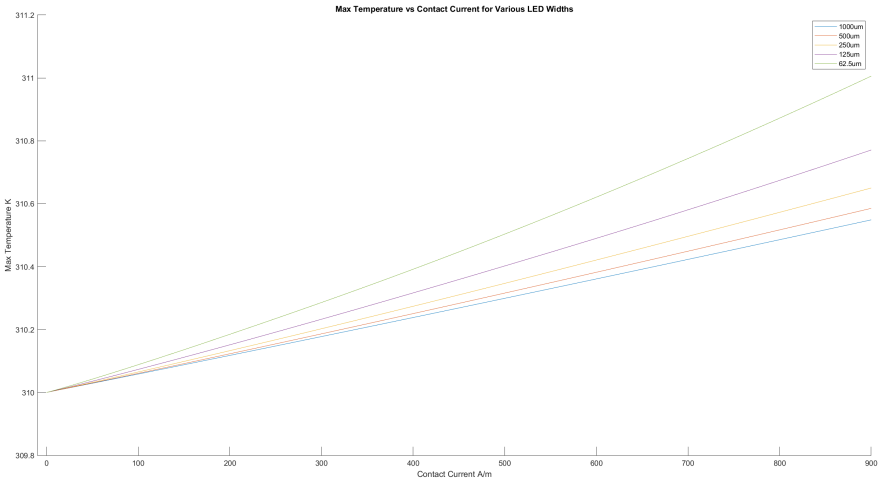


Figure 8: Max Temperature vs Current Injection for 1210 nm LED with Various Device Widths

Output Power is a key performance metric of the device, as its total output power corresponds directly with the resolution available for photoacoustic imaging. As the injected current increases, the output power increases. In addition, larger devices perform better than smaller devices for output power. However, one can fit multiple smaller devices in the same area as a large device, presenting a trade-off. A plot of output power vs. current injection can be seen below in Figure 9

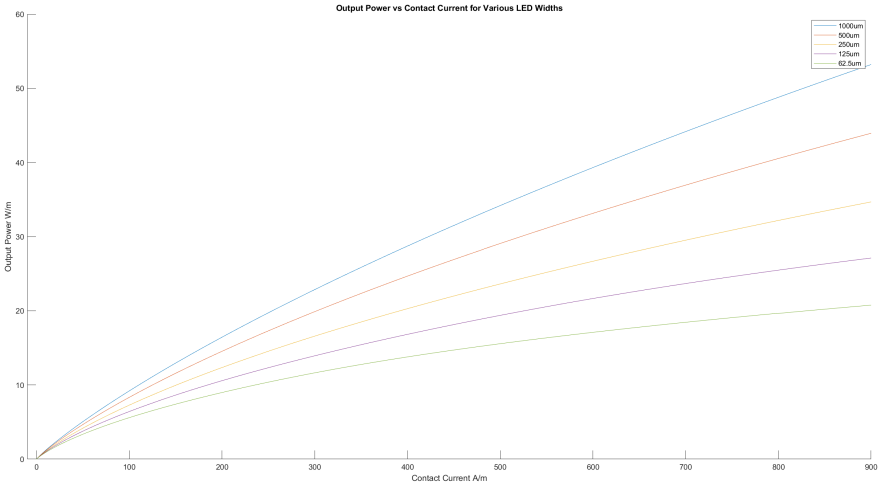


Figure 9: Total Power vs Current Injection for 1210 nm LED with Various Device Widths

## IV.3 Tabulation on Viable Devices

This section tabulates the various temperature and power output metrics for each wavelength output performed. There is no exact numerical value for acceptable temperature and necessary output, however throughout most articles there seems to be a consensus that 500 ns pulse is the longest possible. Temperature was limited to a change in 5 K, this is to prevent noise from ultrasonic waves generated by the LED device itself.

Analyzing the criteria for the 530 nm LEDs, the 250 and 500 um LED sizes meet criteria.

| $\lambda$ (nm) | $W$ (um) | $T$ (K) | $\tilde{P}$ (W/m) | $P$ (mW) | 50ns (uJ) | 100ns (uJ) | 500ns (uJ) |
|---|---|---|---|---|---|---|---|
| 530 | 62.5 | 318.03 | 351.27 | 21.95 | 0.281 | 0.562 | 2.81 |
| 530 | 125 | 315.54 | 417.82 | 52.23 | 0.167 | 0.334 | 1.67 |
| 530 | 250 | 313.97 | 490.11 | 122.53 | 0.098 | 0.196 | 0.98 |
| 530 | 500 | 313.00 | 577.34 | 288.67 | 0.057 | 0.116 | 0.577 |
| 530 | 1000 | 312.42 | 665.62 | 665.62 | 0.033 | 0.066 | 0.333 |

Table 3: Results for 530 nm devices

Analyzing the criteria for the 630 nm LEDs, the 250 um LED size meet criteria.

| $\lambda$ (nm) | $W$ (um) | $T$ (K) | $\tilde{P}$ (W/m) | $P$ (mW) | 50ns (uJ) | 100ns (uJ) | 500ns (uJ) |
|---|---|---|---|---|---|---|---|
| 630 | 62.5 | 318.69 | 219.20 | 13.70 | 0.175 | 0.350 | 1.753 |
| 630 | 125 | 316.19 | 269.57 | 33.69 | 0.107 | 0.215 | 1.076 |
| 630 | 250 | 314.62 | 323.69 | 80.92 | 0.064 | 0.129 | 0.647 |
| 630 | 500 | 313.08 | 452.38 | 226.19 | 0.045 | 0.091 | 0.452 |
| 630 | 1000 | 313.07 | 454.77 | 454.77 | .0227 | 0.046 | 0.227 |

Table 4: Results for 630 nm devices

Analyzing the criteria for the 1070 nm LEDs, the 62.5 and 125 um LED size meet criteria.

| $\lambda$ (nm) | $W$ (um) | $T$ (K) | $\tilde{P}$ (W/m) | $P$ (mW) | 50ns (uJ) | 100ns (uJ) | 500ns (uJ) |
|---|---|---|---|---|---|---|---|
| 1070 | 62.5 | 310.67 | 99.97 | 6.25 | 0.080 | 0.160 | 0.7998 |
| 1070 | 125 | 310.47 | 127.42 | 15.93 | 0.051 | 0.102 | 0.510 |
| 1070 | 250 | 310.42 | 158.54 | 39.64 | 0.032 | 0.063 | 0.317 |
| 1070 | 500 | 310.47 | 174.08 | 87.04 | 0.017 | 0.035 | 0.174 |
| 1070 | 1000 | 310.38 | 218.24 | 218.24 | 0.011 | 0.022 | 0.109 |

Table 5: Results for 1070 nm devices

Analyzing the criteria for the 1210 nm LEDs, none of the LEDs meet criteria.

| $\lambda$ (nm) | $W$ (um) | $T$ (K) | $\tilde{P}$ (W/m) | $P$ (mW) | 50ns (uJ) | 100ns (uJ) | 500ns (uJ) |
|---|---|---|---|---|---|---|---|
| 1210 | 62.5 | 311.01 | 20.76 | 1.30 | 0.017 | 0.033 | 0.166 |
| 1210 | 125 | 310.77 | 27.12 | 3.39 | 0.011 | 0.022 | 0.109 |
| 1210 | 250 | 310.65 | 34.68 | 8.67 | 0.007 | 0.014 | 0.069 |
| 1210 | 500 | 310.59 | 43.94 | 21.97 | 0.004 | 0.008 | 0.044 |
| 1210 | 1000 | 310.55 | 53.21 | 53.21 | 0.003 | 0.005 | 0.027 |

Table 6: Results for 1210 nm devices

There are a few simulated LEDs that are potential candidates for intravascular photoacoustic imaging. One interesting result from this data is the poor performance of the 1210 nm LED. Previous studies [18] have also observed poor optical intensity for 1210 nm InGaAs devices compared to shorter wavelengths, however the behavior in the simulations seems to be magnified a few times. A potential solution to this issue is the use of additional QW confining layers to help promote recombination, however, this behavior proved too difficult to simulate. An additional point of interest is the dramatic temperature difference between the devices, likely attributed to the lower optical output of the devices comparatively.

# V Conclusion

With newer medical imaging techniques requiring large machines and high costs, an alternative cheaper form is needed to increase availability. Photoacoustic systems relying on lasers are reaching their limit on cost reduction and therefore, an alternative form of illumination in the form of LEDs is being researched. LEDs provide both cost benefits being cheaper to fabricate and also safety benefits as they have lower power output.

In this paper, a photoacoustic LED capable of intravascular photoacoustic imaging is explored. The various trends and trade-offs between current injection and device size are investigated for a wide range of values. These trends revealed the impact that sizing effects, current droop, and recombination have on a device. Determining an optimal balance between the temperature, power output, and size proved to be a difficult challenge. The end result recommended a variety device, providing flexibility with different options depending on the LEDs application.

To improve the accuracy of this report, a more detailed model for the thermal behavior of the device needs to be introduced. In addition, the effect of temperature on both radiative and non-radiative recombination would provide a more accurate understanding of the device behavior. The simulations performed in this report were using a 2-dimensional object, perhaps by scaling to 3-dimensions the thermal behavior in the center of the device alongside a continuous heat sink could provide important further insight into the feasibility of this device operating in the real world. Lastly power output improvements in the near-infrared wavelengths, would prove beneficial enabling better imaging at a greater depth.

# Bibliography


[1] E. Bercovich and M. C. Javitt, "Medical imaging: From roentgen to the digital revolution, and beyond," *Rambam Maimonides Medical Journal*, vol. 9, no. 4, p. e0034, Oct. 2018. [Online]. Available: http://dx.doi.org/10.5041/RMMJ.10355

[2] Panchbhai and A. S., "Wilhelm conrad röntgen and the discovery of x-rays: Revisited after centennial," *Journal of Indian Academy of Oral Medicine and Radiology*, vol. 27, no. 1, p. 90, 2015. [Online]. Available: http://dx.doi.org/10.4103/0972-1363.167119

[3] O. for Economic Cooperation and Development, *Health at a Glance 2023*. OECD, Nov. 2023. [Online]. Available: http://dx.doi.org/10.1787/19991312

[4] A. Ignee, N. S. Atkinson, G. Schuessler, and C. Dietrich, "Ultrasound contrast agents," *Endoscopic Ultrasound*, vol. 5, no. 6, p. 355, 2016. [Online]. Available: http://dx.doi.org/10.4103/2303-9027.193594

[5] P. Beard, "Biomedical photoacoustic imaging," *Interface Focus*, vol. 1, no. 4, p. 602–631, Jun. 2011. [Online]. Available: http://dx.doi.org/10.1098/rsfs.2011.0028

[6] J. Xia, J. Yao, and L. H. V. Wang, "Photoacoustic tomography: Principles and advances (invited review)," *Progress In Electromagnetics Research*, vol. 147, p. 1–22, 2014. [Online]. Available: http://dx.doi.org/10.2528/pier14032303

[7] Y. Zhu, T. Feng, Q. Cheng, X. Wang, S. Du, N. Sato, J. Yuan, and M. Kuniyil Ajith Singh, "Towards clinical translation of led-based photoacoustic imaging: A review," *Sensors*, vol. 20, no. 9, p. 2484, Apr. 2020. [Online]. Available: http://dx.doi.org/10.3390/s20092484

[8] B. Wang, J. L. Su, A. B. Karpiouk, K. V. Sokolov, R. W. Smalling, and S. Y. Emelianov, "Intravascular photoacoustic imaging," *IEEE Journal of Selected Topics in Quantum Electronics*, vol. 16, no. 3, p. 588–599, 2010. [Online]. Available: http://dx.doi.org/10.1109/JSTQE.2009.2037023

[9] B. Streetman and S. Banerjee, *Solid State Electronic Devices Seventh Edition*. Pearson Education, Feb. 2014.

[10] R. Stratton, "Semiconductor current-flow equations (diffusion and degeneracy)," *IEEE Transactions on Electron Devices*, vol. 19, no. 12, p. 1288–1292, Dec. 1972. [Online]. Available: http://dx.doi.org/10.1109/T-ED.1972.17592

[11] B. Shrestha, F. DeLuna, M. A. Anastasio, J. Yong Ye, and E. M. Brey, "Photoacoustic imaging in tissue engineering and regenerative medicine," *Tissue Engineering Part B: Reviews*, vol. 26, no. 1, p. 79–102, Feb. 2020. [Online]. Available: http://dx.doi.org/10.1089/ten.teb.2019.0296

[12] A. Verma, S. J. Asivatham, T. Deneke, Q. Castellvi, and R. E. Neal, "Primer on pulsed electrical field ablation: Understanding the benefits and limitations," *Circulation: Arrhythmia and Electrophysiology*, vol. 14, no. 9, Sep. 2021. [Online]. Available: http://dx.doi.org/10.1161/CIRCEP.121.010086

[13] D. Jung, S. Park, C. Lee, and H. Kim, "Recent progress on near-infrared photoacoustic imaging: Imaging modality and organic semiconducting agents," *Polymers*, vol. 11, no. 10, p. 1693, Oct. 2019. [Online]. Available: http://dx.doi.org/10.3390/polym11101693

[14] V. Perekatova, P. Subochev, M. Kleshnin, and I. Turchin, "Optimal wavelengths for optoacoustic measurements of blood oxygen saturation in biological tissues," *Biomedical Optics Express*, vol. 7, no. 10, p. 3979, Sep. 2016. [Online]. Available: http://dx.doi.org/10.1364/BOE.7.003979

[15] D. E. Aspnes, S. M. Kelso, R. A. Logan, and R. Bhat, "Optical properties of alxga1-x as," *Journal of Applied Physics*, vol. 60, no. 2, p. 754–767, Jul. 1986. [Online]. Available: http://dx.doi.org/10.1063/1.337426

[16] A. S. Barker and M. Ilegems, "Infrared lattice vibrations and free-electron dispersion in gan," *Phys. Rev. B*, vol. 7, pp. 743–750, Jan 1973. [Online]. Available: https://link.aps.org/doi/10.1103/PhysRevB.7.743

[17] M. A. Elblbesy, "The refractive index of human blood measured at the visible spectral region by single-fiber reflectance spectroscopy," *AIMS Biophysics*, vol. 8, no. 1, pp. 57–65, 2021. [Online]. Available: https://www.aimspress.com/article/doi/10.3934/biophy.2021004

[18] N. Tansu, J.-Y. Yeh, and L. J. Mawst, "Extremely low threshold-current-density InGaAs quantum-well lasers with emission wavelength of 1215-1233 nm," *Applied Physics Letters*, vol. 82, no. 23, pp. 4038–4040, 06 2003. [Online]. Available: https://doi.org/10.1063/1.1581978